ACS APPLIED MATERIALS & INTERFACES

www.acsami.org Research Article

Temperature-Dependent Carrier Extraction and the Effects of Excitons on Emission and Photovoltaic Performance in $Cs_{0.05}FA_{0.79}MA_{0.16}Pb(I_{0.83}Br_{0.17})_3$ Solar Cells

Hadi Afshari,* Brandon K. Durant, Ahmad R. Kirmani, Sergio A. Chacon, John Mahoney, Vincent R. Whiteside, Rebecca A. Scheidt, Matthew C. Beard, Joseph M. Luther, and Ian R. Sellers*

Cite This: https://doi.org/10.1021/acsami.2c11657 Read Online

ABSTRACT: The photovoltaic parameters of triple cation perovskite [$Cs_{0.05}FA_{0.79}MA_{0.16}Pb(I_{0.83}Br_{0.17})_3$] solar cells are investigated focusing on the electro-optical properties and differences in performance at low and high temperatures. The signature of a parasitic barrier to carrier extraction is observed at low temperatures, which results in a loss of performance at $T < 200$ K. Intensity-dependent measurements indicate extraction across this parasitic interface is limited by a combination of the exciton binding energy and thermionic emission. However, the photovoltaic performance of the device is recovered at low intensity—where the photocarrier generation rate threshold is lower than the thermionic extraction rate. Loss of solar cell performance is also observed to be strongly correlated to an increase in photoluminescence intensity, indicating inhibited carrier extraction results in strong radiative recombination and that these systems do not appear to be limited by significant thermally activated non-radiative processes. Evidence of limited carrier extraction due to excitonic effects is also observed with a strong anti-correlation in photoluminescence and carrier extraction observed at lower temperatures.

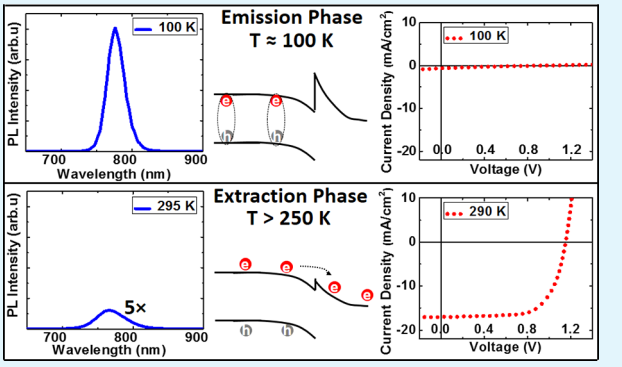

KEYWORDS: *solar cell, perovskites, low temperatures, excitons, carrier extraction, barrier*

1. INTRODUCTION

The relatively poor stability of perovskite solar cells is the major challenge preventing this emerging technology from instantaneous success. However, stability issues are not only due to the perovskite absorber layer, instability can also be rooted in other layers and/or at interfaces within the solar cell architecture.[1,2] Charge transport layers have been recognized to be the source of some instabilities, and studies focused on the improvement of these layers have enhanced the performance of perovskite cells in terms of both stability and efficiency.[3−5] In the case of electron transport layers (ETLs), metal oxides, such as TiO_2 and SnO_2, were shown to result in perovskite cells with improved thermal stability.[6−9] The evolution of these systems has also seen the incorporation of thin organic and/or dielectric layers to stabilize the interface and improve interfacial properties.[10,11]

The loss of performance of the photovoltaic parameters in a perovskite solar cell helps inform which mechanism or region is responsible for degradation of the device. The degradation pattern of perovskite solar cells over their lifetime is qualitatively similar to experiencing an initial exponential decay of the efficiency of the solar cell followed by a linear regime.[1,12] The initial exponential decay phase—or performance—can be recovered by keeping the device in the dark for a few hours or days. The general consensus is that the migration of cation vacancies causes this short-term effect. Accumulation of such defects results in creation of a Debye layer at the interface with the ETL, which in turn inhibits charge extraction.[13] The second decay phase (linear) is not reversible and is correlated with permanent degradation processes.[1]

In terms of the hole transport layer (HTL), poly[bis(4-phenyl)(2,4,6-trimethylphenyl)amine] (PTAA) and 2,2′,7,7′-tetrakis(N,N-di-p-methoxyphenyl-amine)9,9′-spirobifluorene (SPIRO) are the two most successful materials that have been used to date. Both SPIRO and PTAA materials have low electrical conductivity in their pristine form, and typically a combination of ionic additives is used to enhance the electrical properties of these films. SPIRO is the dominant HTL used in perovskite solar cells resulting in the highest efficiency devices

Received: June 30, 2022
Accepted: September 13, 2022

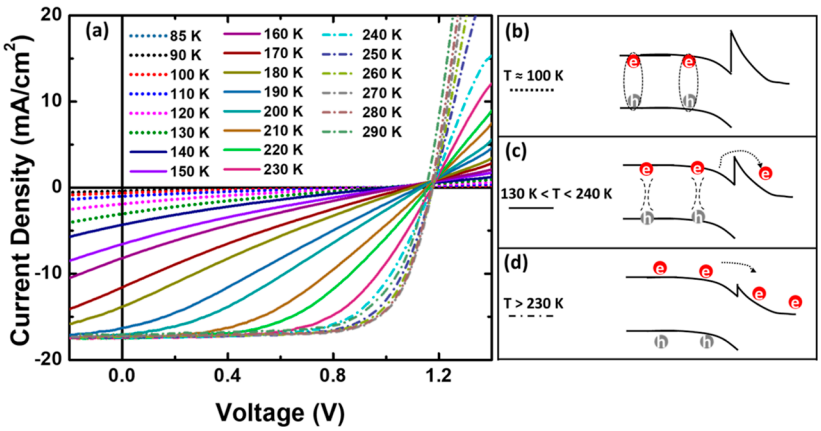

Figure 1. (a) Temperature-dependent $J-V$ measurement. (b−d) Schematic illustrations of the proposed carrier extraction of charge carriers and excitons in the respective temperature regimes in which carrier extraction is perturbed by exciton recombination, thermionic emission, and their thermal energy at 100 K, 140 K−250 K, and at room temperature, respectively.

to date.[3,14,15] However, the lack of long-term stability of doped SPIRO further complicates stability issues.[16,17]

Another phenomena, which affects the electro-optical properties of perovskites, specifically at low temperatures, is the formation and propagation of excitons in these systems.[18] The optical properties of perovskite materials are dominated by excitons of varying strength, which can be traced back to the dielectric constant and geometry of the perovskite crystal lattice.[19−23] Indeed, excitons are responsible for the very large absorption coefficients close to the band gap and the strong radiative emission evident in these systems.[18] Since free charge carriers and excitons have different transport properties, it is important that the dynamics of these transport properties[19] are understood and accounted for. Moreover, in the case of perovskites, the band-edge states are highly affected by the presence of excitons which will be shown—have implications for the performance of perovskite solar cells and the transport properties therein. Understanding the implications of such dynamics in such systems is important to facilitate their commercialization.

Normally, excitonic effects in semiconductor devices are manifested at lower temperatures where carriers do not typically have enough thermal energy to bridge between the band-edge and excitonic states.[24] As such, low-temperature PV measurements provide an "ideal" setting to investigate and understand excitonic effects in the perovskites. Surprisingly, there are few studies of perovskite solar cells at low temperatures, as well as on correlations between the recombination dynamics and carrier transport in these regimes. This is mainly due to the fact that terrestrial solar panels operate at around 300 K; therefore, the predominant focus of the PV community is in realizing stable perovskite solar cells that work at ambient temperatures. However, low-temperature measurements can provide useful information with respect to the physics driving solar cell performance and the role of parasitic processes in performance, stability, and lifetime.

For non-terrestrial applications, such as a satellite power generation system, several additional considerations are required that are dictated by the environment. In space, some environmental effects include: reduced pressure, extreme temperatures, and high irradiation levels. Therefore, solar panels operating in space need to withstand all such conditions.

Recently, space applications of perovskite solar cells have gained attention due to the relatively high radiation tolerance of these systems in space conditions.[25−28] The radiation tolerance of the perovskite material is rooted in the soft nature of this system and the flexible crystal structure. However, due to the thermal regimes, such systems working within the space environment would swing from low to high temperatures (as low as 100 K); hence, there is a need to study the low-temperature operation of perovskite solar cells for such applications.[29] Here, the low-temperature behavior of the triple cation $Cs_{0.05}FA_{0.79}MA_{0.16}Pb(I_{0.83}Br_{0.17})_3$ perovskite solar cells are investigated, and the evolution of their properties monitored as the solar cell experiences thermal regimes from low to high (room) temperatures.

2. EXPERIMENTAL SECTION

The devices were fabricated on ITO coated Ce-borosilicate substrates with dimensions of 25.4 mm × 25.4 mm × 0.25 mm and completed with a thermal evaporation of 100 nm gold contacts. The full details of the fabrication process are described in the Supporting Information. A Keithley 2400 multimeter is used as a voltage source to apply stepwise discrete bias values scanning in forward and reverse directions while simultaneously measuring the resultant current. Current density is calculated by dividing the measured current by the device area illuminated through a mask. The perovskite solar cells were mounted and connected in a Linkam cryostat using a LNP95 cooling system and a T95 temperature controller for temperature-dependent measurements from 85 to 290 K. A Newport Oriel Sol2A solar simulator was used to provide an AM 1.5G solar spectrum. The illumination power density of the solar simulator is calibrated with a silicon reference cell. To perform external quantum efficiency (EQE) measurements, an Oriel Quartz Tungsten Halogen (QTH) lamp was used as the light source with an Oriel Cornerstone 260 monochromator to disperse the excitation source. This system also included a filter wheel with long pass filters to exclude second order light, the measurements were taken using an optical chopper. The signal is collected with a Stanford Research Systems SR830 lock-in amplifier. Two lenses were used to collimate and focus the light onto the sample and an Oriel Si detector used to measure the reference spectrum from 300 nm to 900 nm.

To perform photoluminescence (PL) measurements the 442 nm line of a Kimmon He−Cd laser was used as the excitation source with power of 6 mW. Considering the area of the aperture, the light intensity is 98 mW/cm^2. Borosilicate Crown Newport lenses and Borofloat 33 flat mirrors were used to focus the laser excitation onto the sample in a Janis SHI-4-5 closed-cycle cryostat (4.2 K−295 K). The light emitted from the sample was then collimated and focused

https://doi.org/10.1021/acsami.2c11657
ACS Appl. Mater. Interfaces XXXX, XXX, XXX−XXX

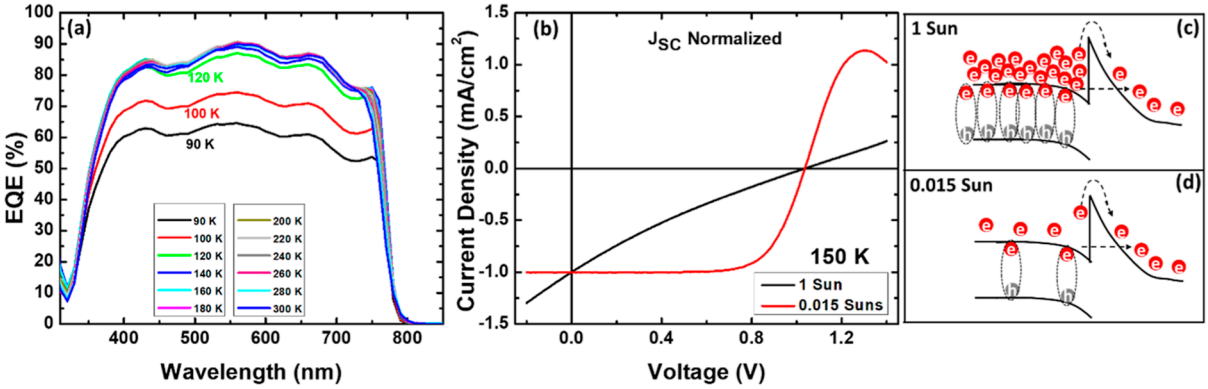

Figure 2. (a) Temperature-dependent EQE. (b) Light $J-V$ results with normalized J_{sc} at 150 K for two different illumination intensities: for 1 sun (black) and for 0.015 sun (red). The schematics in (c,d) illustrate the build-up in excess carrier concentration at 1 sun AM0 at low temperatures due to the low thermionic emission and inhibited carrier extraction, and the higher extraction of low carrier densities at 0.015 sun at the same temperature due to the improve balance in carrier generation and thermionic extraction at lower fluences, respectively.

into a Princeton Instruments Acton SP2500 spectrometer fitted with an air-cooled Si charge coupled device (2-dimensional CCD array). Winspec data acquisition software is used to control and record the PL data. After mounting the sample into a cryostat, a turbo molecular pump is used to pump down the cryostat to ~5 × 10^{-5} torr and a helium compressor is used to cool the sample to 4.2 K. A heater element attached to a copper cold finger inside the cryostat is controlled by a Lakeshore model 335 temperature controller to vary the temperature of the sample for temperature-dependent measurements.

3. RESULTS AND DISCUSSION

In this structure, the perovskite absorber layer is sandwiched between SnO_2 ETL and a SPIRO HTL. MoO_3 is deposited on top of the SPIRO to improve the interfacial properties, prevent diffusion between the HTL and metal contact, as well as improve carrier extraction. The structure of the solar cell and respective thicknesses of each layer are shown in the Figure S1a. Thicknesses are optimized to provide maximum performance with these materials. The n-type and p-type contacts are SnO_2 and SPIRO, respectively. Supplementary Figure S1b depicts the band alignment of the system. The energy band gap of the $Cs_{0.05}FA_{0.79}MA_{0.16}Pb(I_{0.83}Br_{0.17})_3$ perovskite absorber used in this study is ~1.62 eV, which forms a heterostructure architecture with the other layers that facilitate the transport of electrons and holes into the electrical contacts of the device.

Figure 1a shows the temperature-dependent light $J-V$ results under AM 1.5G illumination measured from 85 K to 290 K. As is evident in this figure at 85 K, the photogenerated short circuit current (J_{sc}) is very small. As the temperature is raised the photocurrent improves gradually, until it reaches a stable saturation point. The same is true for the fill factor (FF) of the solar cell. The photocurrent shows a strong voltage dependence at lower temperatures with a concomitant low FF, suggesting the presence of a barrier to carrier extraction and/or pinning of the Fermi level at low temperatures. Figure 1b−d illustrates the suggested barrier and the role of excitons at various temperatures. In addition to a low photogenerated current and FF, extraction of majority carriers is also inhibited at low temperature as reflected in the small current values above the V_{oc} point. The fact that both minority and majority carrier transport is inhibited suggests that one or more layers is failing to conduct, or an interface barrier is inhibiting the passage of carriers, both of which translates to additional series resistance in the system. The reduced J_{sc} and other PV parameters at very low temperatures has been attributed to the change in electronic properties and morphology of the charge transport layers.[30] For perovskite solar cells to perform well at low temperature such as space, both the perovskite absorber and the constituent transport and interfacial layers must be considered.

The dotted lines in Figure 1a represent the low-temperature regime schematically illustrated in Figure 1b, where carrier transport and extraction are perturbed by both the excitonic nature of the system, and the large barrier to photogenerated carriers in this low thermal energy regime ($T \leq 100$ K). The solid lines in Figure 1a represent an intermediate regime between $T \sim 140$ K and $T \sim 250$ K, whereby the ionization and thermal energy increases the ability of carriers to be successfully collected in the solar cell, which is represented by the enhanced extraction shown schematically in Figure 1c. Figure 1d shows the optimum regime for carrier extraction and efficient PV operation at $T > 250$ K—indicated as lines and symbols in Figure 1a. At $T > 250$ K, the limited barrier to free photogenerated carriers in the perovskite solar cell structure results in low resistance to carrier transport, as well as large currents and voltages under illumination with a high FF.

Figure 2a shows the temperature-dependent EQE from 90 K to 300 K. The EQE spectra generally retain their shape but suffer a reduced magnitude at low temperatures, the EQE increases as the temperature increases further indicating inhibited carrier extraction at low temperatures. This is consistent with that of the J_{sc} response, as expected. Since there is a uniform loss of EQE with temperature, it suggests a barrier to all minority carriers exists in the structure. This is typical of a parasitic barrier at the absorber transport layer interface, where the diffusion and then extraction of all carriers is perturbed. Although the qualitative trend of the EQE and J_{sc} are consistent, there is a notable quantitative discrepancy between the EQE and J_{sc} results: the low-temperature EQE results show a greater extraction efficiency at lower temperatures (Figure 2a), while the J_{sc} extracted from the 1 sun $J-V$ indicates negligible charge extraction (see Figure 1a and 3b). Specifically, at $T = 90$ K, the light $J-V$ measurement gives a J_{sc} of 0.45 mA/cm^2; however, the J_{sc} value extracted from the EQE measurement ($T = 90$ K) is ~14 mA/cm^2.

It is worth noting that there are differences between the measurements that could account for some discrepancy. The difference between light sources used for EQE and $J-V$

https://doi.org/10.1021/acsami.2c11657
ACS Appl. Mater. Interfaces XXXX, XXX, XXX−XXX

measurements include: mono wavelength light in an EQE measurement, which scans over a broad spectrum (here from 300 nm to 1100 nm), while the $J-V$ is measured under an AM 1.5G spectrum comprising all the wavelengths of this broadband solar spectrum. Moreover, the intensity of the optical excitation in the EQE measurement is significantly lower than that of AM 1.5G from the solar simulator. These differences can affect the role of defects and non-idealities in carrier extraction via the passivation of defects or the lack thereof as well as to affect recombination under various intensities or under broadband illumination.

To assess the contribution of the intensity on the performance of the solar cells, the light intensity of the solar simulator was reduced to a value qualitatively similar to that of the EQE system (0.015 sun). $J-V$ measurements were then performed at 150 K, where J_{sc} and V_{oc} values have not reached a maximum and the response of the system is low under full 1 sun intensity (see Figures 1a and 3b). Figure 2b shows the normalized (J_{sc}) comparison of the light $J-V$ measurements performed under 1 sun and 0.015 sun at 150 K. While the $J-V$ response of the cell under AM 1.5G has almost no rectifying behavior and resembles the response of a resistor; under 0.015 sun, the photovoltaic parameters are restored. Interestingly, despite the intensity difference V_{oc} is not changed under high (or low) fluence, indicating the major role of inhibited carrier extraction is to limit carrier collection and not to enhance parasitic recombination losses (the unnormalized data is shown in supplementary Figure S2, further demonstrating this effect).

The intensity dependence of the $J-V$ measurements, coupled with the monotonic reduction in the EQE spectrum with temperature further support the presence of a parasitic barrier at an interface and inhibiting carrier transport. In this scenario, carrier extraction is a result of two competing factors: photogeneration and thermionic emission of carriers.

For high incident illumination, the photogeneration rate exceeds thermionic emission across the parasitic barrier at low temperatures, as such only a fraction of photogenerated carriers can pass the interface—translating to a low FF and therefore low power conversion efficiency, an operational situation schematically illustrated in Figure 2c. However, as the intensity of the light (therefore the photo-generation rate) is reduced, the ability of the thermionic emission to extract carriers increases resulting in an improved FF and efficiency of the solar cell, as illustrated in Figure 2d. This behavior implies that at low temperatures the extraction rate is constant and higher illumination does not lead to higher extraction—this translates in a lower efficiency for higher illumination intensities in the presence of a parasitic barrier. These data are consistent with previous results on perovskite solar cells under LILT conditions.[31]

Further evidence of the presence of a barrier to carrier extraction is evident in the $J-V$ shown in Figure 2b at a higher applied bias. The roll over or negative differential resistance observed at ~1.2 V is a typical response in perovskite solar cells when applying large voltages to the cell and represent tunnel currents at the heterointerface between the perovskite absorber and/or the transporting layers. This illustrates the unique operating principle of perovskite solar cell devices in general: solar cells which experience their rectification from the diffusion of charge carriers across the intrinsic perovskite region and selective extraction via a high field Schottky-like process that extracts majority electrons (rejects minority holes) preferentially at the respective hetero-interfaces.[32] Large applied voltages perturb efficiency of such extraction through the creation of large barriers and inhibited thermionic extraction.[33,34]

Figure 3a shows the temperature-dependent PL from 4.2 K to 295 K (the dotted line is a guide for the eye). As the

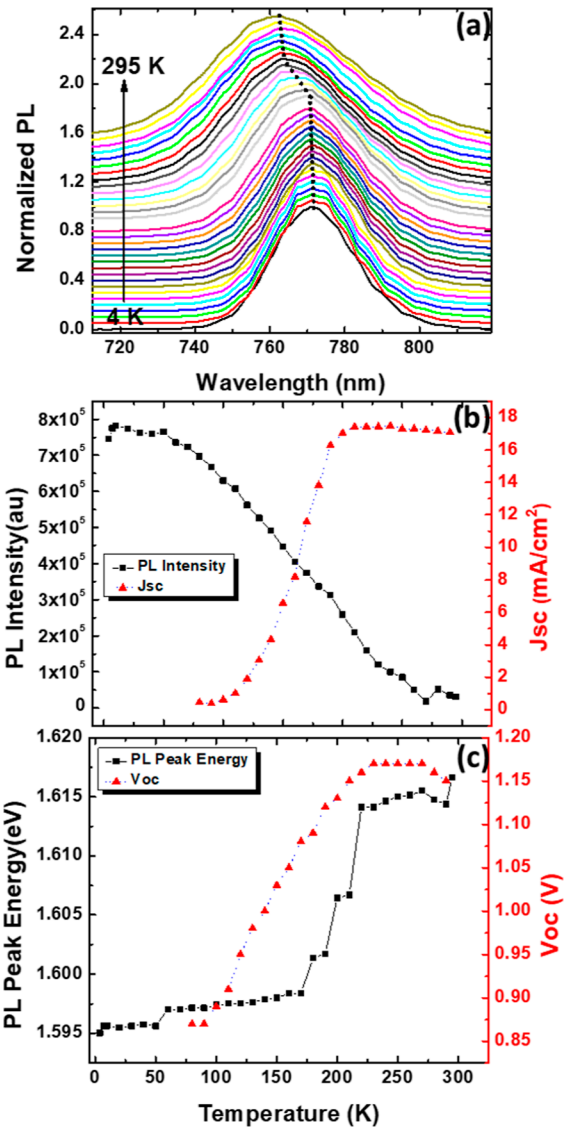

Figure 3. (a) Temperature-dependent photoluminescence of the solar cell from 4 K to 295 K. The dotted line is a guide for the eye. (b) Integrated intensity extracted from (a) and J_{sc} extracted from Figure 1a as a function of temperature. (c) Peak energy from 3(a) and V_{oc} from Figure 1a as a function of temperature.

temperature is raised, the PL intensity reduces, peak energy experiences a blue shift, and the spectra broadens. This is further illustrated in Figure 3b, which shows the integrated intensity of the PL as a function of temperature taken from the data (solid black squares) in Figure 3a. The blue shift in the PL peak energy is associated with the increase of the band gap of the perovskite material with temperature due to the well-known and unique band structure of metal halide perovskites (this is opposite to III−V semiconductors or silicon). The broadening of the PL can be well understood in terms of increased Fröhlich interaction at $T > 30$ K.[35] The origin of the

https://doi.org/10.1021/acsami.2c11657
ACS Appl. Mater. Interfaces XXXX, XXX, XXX−XXX

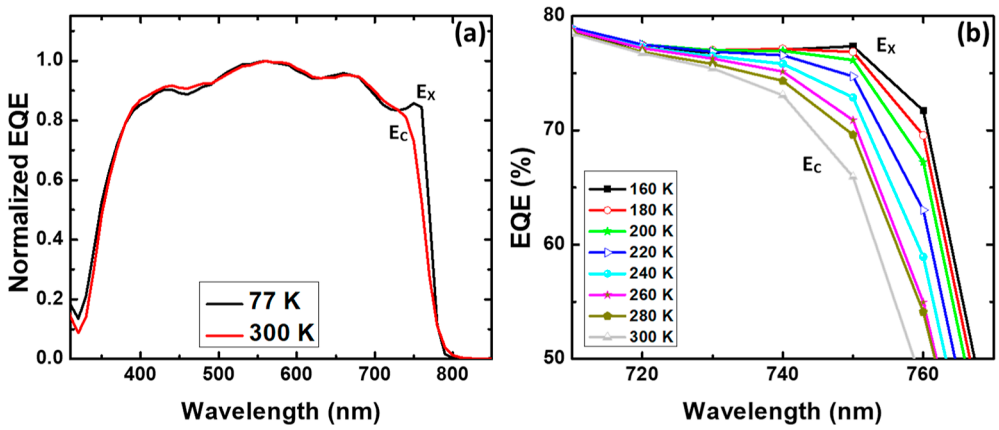

Figure 4. (a) EQE of the solar cell at 77 K and 300 K, normalized to the room-temperature EQE. (b) Temperature-dependent EQE, expanded view of the exciton region.

decrease in the radiative efficiency of the perovskite does not appear to be dominated by the activation of non-radiative losses but rather, the result of improved carrier extraction and improved device performance at elevated temperatures. This is evident when compared to the temperature dependence of the J_{sc} (solid red triangles) in Figure 3b which between 85 K−100 K is negligible (∼0.3 mA/cm^2). Whilst after 100 K, it rises rapidly reaching approximate saturation at ∼200 K.

Figure 3b,c shows J_{sc} and V_{oc} values extracted from Figure 1a. Here, both V_{oc} and J_{sc} are shown to have low values at low temperatures and improve with increasing temperature. Both these parameters reach a stable maximum between 200 K and 220 K. The reduction in V_{oc} implies that there is a voltage drop at one of the interfaces. This effect is likely due to the temperature dependence of the constituent layers leading to the creation of barriers at various interfaces at low temperatures, which are removed at $T > 200$ K (which is considerably less than the typical operating temperature of such solar cells). In perovskite solar cells, a loss of FF at low temperature has also been attributed to inhibited carrier transport in the perovskite absorber layer,[36] non-ideal heterojunction offsets, and low conductivity of the transport layers at low temperatures.[37] This is discussed further below.

When considering the loss of PL intensity and extracted photocurrent there appears an (anti) correlation in the intensity of the PL with the carrier extraction (J_{sc}). This loss in PL is a direct consequence of the rapid extraction of photogenerated carriers between 100 K and 200 K. Furthermore, the small and approximately constant PL at $T > 250$ K—when the solar cell has reached its optimum performance (see Figure 1)—indicates the solar cell remains predominantly within the radiative limit and that carriers not collected recombine radiatively. This is also supported by the large and the unusual temperature dependence of the V_{oc} (∼1.15 V) evident above 200 K, as shown in Figure 3c. At $T \sim 85$ K, V_{oc} is ∼0.85 V increasing to 1.15 V at 200 K when it stabilizes up to room temperature.

Typically, non-radiative processes manifest themselves in an increase in the dark current and subsequent loss of V_{oc}. Since the temperature-dependent reduction in PL does not result in simultaneous loss of V_{oc}, the limited performance of the device at lower temperatures can be unambiguously attributed to the role of parasitic barriers, low thermal energy of carriers, and the non-ideality of current extraction due to lower thermionic emission at high excitation. Furthermore, since the band gap of perovskites increases at higher temperatures (rather than decreasing in typical III−V semiconductors), the increased voltage also likely represents the increasing band gap of the absorber, coupled with more optimum band offsets at $T > 200$ K. This hypothesis is consistent with the temperature-dependent dark $J-V$ data shown in supplementary Figures S3 and S4, which show very high resistance against carrier extraction at low temperatures, an indication of some barrier to extraction at such temperatures. The carrier transport improves at elevated temperatures.

The effect of the temperature on the band gap can be more clearly observed in Figure 3c, which shows a comparison of the temperature dependence of the V_{oc}, and the peak PL energy extracted from the PL data in Figure 3a. These data can also be compared to the temperature-dependent PL intensity and J_{sc} shown in Figure 3b, as they are plotted on the same temperature axis. The PL data shown in Figure 3c indicates that excitonic effects also play a strong role in the performance of the solar cells. In addition to the parasitic barriers evident at $T < 200$ K, the carrier transport/extraction is also inhibited at lower temperatures by excitonic complexes or the large binding energy of excitons in the triple cation perovskite system under investigation here. When considering the dependence of the peak PL energy in Figure 3c with temperature (solid black squares), a steady increase in the energy is observed consistent with a thermally mediated increase in the band gap of the $Cs_{0.05}FA_{0.79}MA_{0.16}Pb(I_{0.83}Br_{0.17})_3$.

At $T \sim 170$ K, an abrupt increase in the PL position from ∼1.597 eV to 1.615 eV is observed. This jump in the PL peak energy is revealed in a significant shift observed in the PL spectra evident in Figure 3a at high temperatures. While perovskite materials are known to undergo phase transitions with increasing temperature,[38−40] this phenomenon is usually accompanied by a sudden reduction of the band gap at the temperature at which the crystallographic transition occurs. This is opposite to the effect observed in Figure 3a, which shows an increase in the peak PL energy. Furthermore, the heat map presented in the supplementary Figure S5 also indicates that this system does not undergo a significant phase transition over the temperature range investigated (4 K to 295 K). This further demonstrates the improved stability for the tailored triple cation perovskite absorber $Cs_{0.05}FA_{0.79}MA_{0.16}Pb(I_{0.83}Br_{0.17})_3$ studied here.[41]

Notably, when comparing the behavior of both the V_{oc} and J_{sc} with temperature in Figure 3b,c, there is a clear

https://doi.org/10.1021/acsami.2c11657
ACS Appl. Mater. Interfaces XXXX, XXX, XXX−XXX

correspondence with the ionization of the excitons—both parameters increase as the excitonic binding energy softens with increasing temperature. Also, the absorption edge blue-shifts above $T \sim 170$ K (see Figure 4b) eventually plateauing at ~ 210 K when the transition to the free excitonic regime is essentially complete and the thermal energy in the system (k_BT) exceeds the exciton binding energy. As such, the increase in peak energy at $T \sim 170$ K observed in the PL spectra is attributed to the ionization of excitons and the subsequent increase in the absorption edge upon annihilation of the excitonic species. This hypothesis is further supported by the EQE shown in Figure 4a, where clear evidence of exciton absorption and the quenching of these effects is apparent when comparing the normalized low (77 K) and high (300 K) temperature EQE. While the excitonic complex, E_X is clear at low temperatures it merges into the continuum, E_C at higher temperatures.

Figure 4b maps the evolution of exciton ionization by magnifying the temperature-dependent EQE over the exciton region for temperatures between 160 K and 300 K. In this figure, the EQE of the solar cell at 160 K shows a peak at the onset of the EQE. At 160 K, the EQE is dominated by the strong excitonic absorption while with increasing temperature there is a weakening and blue shift of the exciton with the emergence and dominance of the continuum at $T > 200$ K. The effect of excitons at low temperatures can also be followed when comparing the emission (PL) and absorption (EQE) at several temperatures across the transition region from excitons to that of free carriers.

Figure 5a−c shows a comparison of the PL and EQE at T = 90 K, 180 K, and 280 K, respectively. Here, only the low energy portion (absorption edge) of the EQE spectra are shown to allow comparison of the broadening of the PL and low energy tail of the EQE to be more readily assessed—the full spectra are shown in Figure 2a. An evolution of the characteristics of the band-edge states and their role in the PL and EQE can be observed. At lower temperatures (90 K), the EQE is dominated by the excitonic nature of the systems as is evident via the strong exciton absorption at the band edge and the narrow and intense PL. As the temperature is increased to ∼180 K [chosen for its proximity to the ionization regime of excitons evident in the PL (Figure 3) and J−V (Figure 1) measurements], the continuum begins to dominate the EQE and the PL broadens [Figure 5b] through a combination of enhanced carrier−phonon interactions, reduced radiative efficiency, and more efficient free carrier extraction. This is reflected in the increase in both J_{sc} and total EQE at higher temperatures (see Figure 2). At the higher temperature (280 K), the EQE is dominated by band-to-band absorption and the associated PL is significantly broadened due to the strong Fröhlich coupling inherent in the metal halide perovskites[42] and the presence of large polarons in the system.[43−46] Such effects have been discussed by several groups demonstrating the significant role of LO phonons play in linewidth broadening (Γ) of the PL in these polar systems.[42,47−49] In the devices presented here the linewidth of the PL increases from Γ ∼ 54 meV at 4 K to Γ ∼ 103 meV at 295 K, analysis of which is given in S6 of the Supporting Information.

The role of the carrier localization via the band offsets at heterointerfaces at lower temperature, and the role of the exciton binding energy on the PL and carrier extraction can be further understood by correlating the temperature-dependent

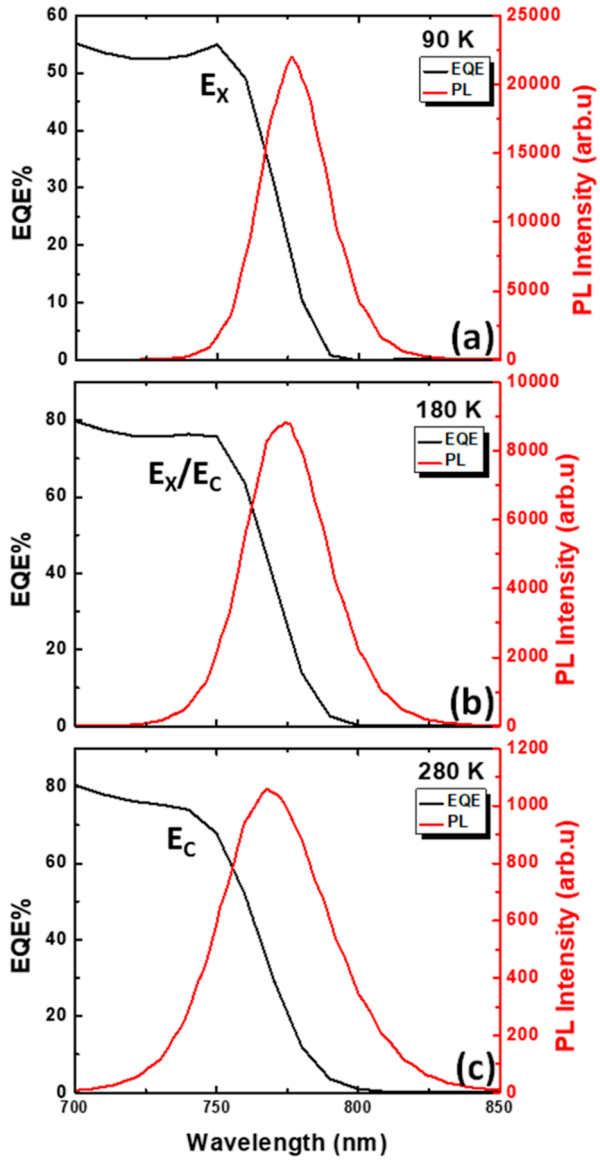

Figure 5. PL and EQE graphs overlaid on each other at temperatures of (a) 90 K, (b) 180 K, and (c) 280 K. The red curve is PL results and the black curve is for EQE.

PL intensity to that of the J_{sc} via complementary Arrhenius analysis. Specifically, for PL

$$I(T) = \frac{I_0}{1 + a \times \exp\left(\frac{-E_x}{k_BT}\right) + b \times \exp\left(\frac{-E_b}{k_BT}\right)} \quad (1)$$

where I_0 represents the integrated PL intensity at 4.2 K; a, b, E_x, and E_b are the coefficients and energies associated with various activation processes. T and k_B represent the temperature and Boltzmann constant, respectively.

Figure 6a shows the plot of the integrated PL intensity versus temperature. An Arrhenius fit is used to extract the activation energies. The data follows (within errors) two activation energies of ∼26 meV and ∼143 meV, which are attributed to the exciton binding energy, E_x, and the contribution of a parasitic barrier (associated with a perovskite/transporting layer), E_b, respectively. The respective roles of these processes is illustrated schematically, as an inset to Figure 6a. While the exciton binding energy extracted here is

https://doi.org/10.1021/acsami.2c11657
ACS Appl. Mater. Interfaces XXXX, XXX, XXX−XXX

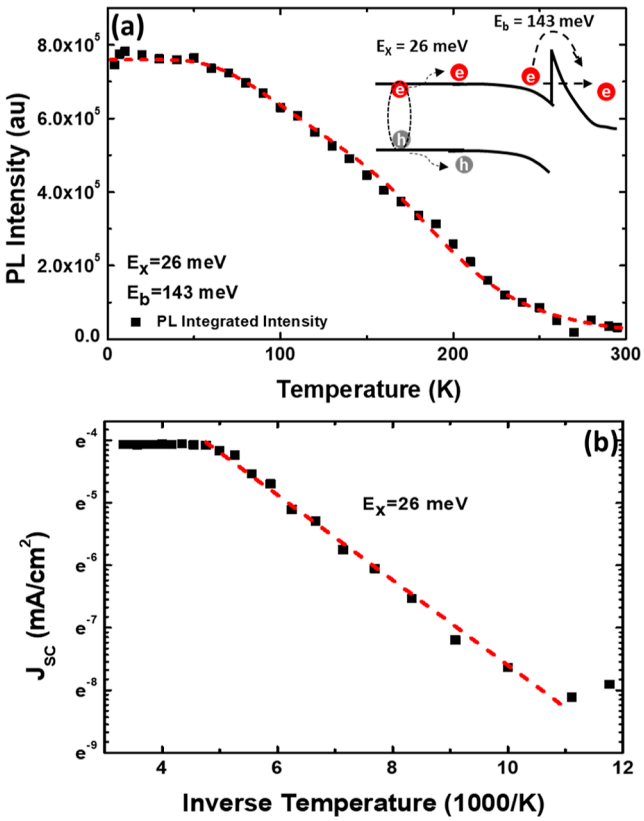

Figure 6. (a) Arrhenius plot of the temperature dependence of the PL-integrated intensity fit with two activation energies. The inset illustrates the effect and relative contribution to carrier extraction as well as, the rate of radiative recombination due to the potential barrier and exciton binding energies in these systems. (b) Arrhenius plot of the J_{sc} vs inverse temperature ($1000/T$) to calculate the activation energy value of excitonic states.

consistent with that determined elsewhere[50−52] for this system, the origin of the specific interface responsible for E_b remains under debate. Its presence and role in the transport and extraction is evident at higher applied voltages at all temperatures (see, e.g., Figure 2b). This results in stable PL at ambient conditions (T > 200 K) despite the high photovoltaic performance of the solar cells at room temperature. While further analysis is required to unambiguously determine the origin of the interface responsible, this is likely related to the MoO_3 layer, which requires efficient tunneling of carriers to limit parasitic resistance and retain effective operation of the perovskite solar cell architecture.[32]

The relationship between the carrier extraction and the PL is further supported by Figure 6b, which shows the ln J_{sc} versus $1000/T$ plot for the perovskite solar cell. The current in the linear region has been found to fit with the Arrhenius equation

$$\ln J_{SC} = \ln J_0 - \left(\frac{E_x}{(k_B \times 1000)}\right)\left(\frac{1000}{T}\right) \quad (2)$$

where J_{sc} is the short circuit current density, E_x is the activation energy of the charge carriers to participate in the conduction process, k_B is the Boltzmann's constant, T is the temperature, and J_0 is the intrinsic current density of the sample. The activation energy is calculated equating the slope of the plot (shown in Figure 6b) with ($E_x/(k_B \times 1000)$). The activation energy extracted from this method also predicts an $E_x \sim 26$ meV consistent with the exciton binding energy, extracted for the Arrhenius plot of the integrated intensity of the PL [Figure 6a]. The relationship between the quenching of the PL intensity with the increase in J_{sc} confirms the conclusion that the change in PL energy observed at ∼170 K has its origin in the transition from excitonic to band-to-band recombination. Despite the inhibited electronic performance at low temperatures, the perovskite solar cells operate predominantly in the radiative limit at all temperatures assessed here.

4. CONCLUSIONS

The temperature dependence of PV parameters of triple cation perovskite [$Cs_{0.05}FA_{0.79}MA_{0.16}Pb(I_{0.83}Br_{0.17})_3$] solar cells was investigated focusing on the electro-optical properties and differences in performance at low and high temperatures. The signature of a parasitic barrier to carrier extraction was observed at low temperatures, which resulted in a loss of performance at T < 200 K. Intensity-dependent measurements indicate extraction across this parasitic interface is limited by a combination of the exciton binding energy and thermionic emission, with the PV parameters recovered at low intensity—where the photo-carrier generation rate threshold is lower than that of the thermionic extraction rate. Loss of solar cell performance was observed to be strongly correlated to an increase in PL intensity, indicating inhibited carrier extraction resulted in strong radiative recombination and that these systems do not appear to be limited significantly by thermally activated non-radiative processes. Evidence of limited carrier extraction due to excitonic effects were also observed with a strong anti-correlation in (high intensity and narrow) PL and (low) carrier extraction observed at lower temperatures. The presence of excitonic absorption in low-temperature EQE and the thermal quenching of this complex indicated excitonic binding energies of ∼26 meV, consistent with values reported by others for the triple cation systems under study here.[52]

■ ASSOCIATED CONTENT

Supporting Information

The Supporting Information is available free of charge at https://pubs.acs.org/doi/10.1021/acsami.2c11657.

Materials and device fabrication sections, structure of the solar cell along with the band alignment, comparison of the light JV results at 150 K for two illumination intensities; 1 sun and 0.015 sun, temperature-dependent dark JV of the solar cell from 85 K up to 290 K, heat map of the temperature-dependent PL from 4 K to 295 K, and linewidth broadening analysis of the temperature-dependent PL (PDF)

■ AUTHOR INFORMATION

Corresponding Authors

Hadi Afshari − *Department of Physics & Astronomy, University of Oklahoma, Norman 73019 Oklahoma, United States;* orcid.org/0000-0001-7984-6313; Email: Hadi.Afshari-1@ou.edu

Ian R. Sellers − *Department of Physics & Astronomy, University of Oklahoma, Norman 73019 Oklahoma, United States;* orcid.org/0000-0003-2782-0044; Email: sellers@ou.edu

Authors

Brandon K. Durant − *Department of Physics & Astronomy, University of Oklahoma, Norman 73019 Oklahoma, United States*

Ahmad R. Kirmani − *National Renewable Energy Laboratory (NREL), Golden 80401 Colorado, United States*

Sergio A. Chacon − *Department of Physics & Astronomy, University of Oklahoma, Norman 73019 Oklahoma, United States*

John Mahoney − *Department of Physics & Astronomy, University of Oklahoma, Norman 73019 Oklahoma, United States*

Vincent R. Whiteside − *Department of Physics & Astronomy, University of Oklahoma, Norman 73019 Oklahoma, United States;* orcid.org/0000-0001-7846-3150

Rebecca A. Scheidt − *National Renewable Energy Laboratory (NREL), Golden 80401 Colorado, United States*

Matthew C. Beard − *National Renewable Energy Laboratory (NREL), Golden 80401 Colorado, United States;* orcid.org/0000-0002-2711-1355

Joseph M. Luther − *National Renewable Energy Laboratory (NREL), Golden 80401 Colorado, United States;* orcid.org/0000-0002-4054-8244

Complete contact information is available at: https://pubs.acs.org/10.1021/acsami.2c11657

Author Contributions

The manuscript was written through contributions of all authors. All authors have given approval to the final version of the manuscript.

Notes

The authors declare no competing financial interest.

■ ACKNOWLEDGMENTS

This work is supported by funding through the National Aeronautics and Space Administration under Agreement no. 80NSSC19M0140 issued through NASA Oklahoma EPSCoR. This work was authored in part by the National Renewable Energy Laboratory, operated by Alliance for Sustainable Energy, LLC, for the U.S. Department of Energy (DOE) under Contract no. DE-AC36-08GO28308. The devices were constructed under the support from the Operational Energy Capability Improvement Fund (OECIF) of the Department of Defense (DOD). The views expressed in the article do not necessarily represent the views of the DOE or the U.S. Government.

■ REFERENCES

(1) Ono, L. K.; Qi, Y.; Liu, S. F. Progress toward Stable Lead Halide Perovskite Solar Cells. *Joule* **2018**, *2*, 1961−1990.

(2) Sutanto, A. A.; Drigo, N.; Queloz, V. I.; Garcia-Benito, I.; Kirmani, A. R.; Richter, L. J.; Schouwink, P. A.; Cho, K. T.; Paek, S.; Nazeeruddin, M. K.; Grancini, G. Dynamical Evolution of the 2d/3d Interface: A Hidden Driver Behind Perovskite Solar Cell Instability. *J. Mater. Chem. A* **2020**, *8*, 2343−2348.

(3) Burschka, J.; Pellet, N.; Moon, S.-J.; Humphry-Baker, R.; Gao, P.; Nazeeruddin, M. K.; Grätzel, M. Sequential Deposition as a Route to High-Performance Perovskite-Sensitized Solar Cells. *Nature* **2013**, *499*, 316−319.

(4) Yang, W. S.; Noh, J. H.; Jeon, N. J.; Kim, Y. C.; Ryu, S.; Seo, J.; Seok, S. I. High-Performance Photovoltaic Perovskite Layers Fabricated through Intramolecular Exchange. *Science* **2015**, *348*, 1234−1237.

(5) Jeon, N. J.; Noh, J. H.; Kim, Y. C.; Yang, W. S.; Ryu, S.; Seok, S. I. Solvent Engineering for High-Performance Inorganic−Organic Hybrid Perovskite Solar Cells. *Nat. Mater.* **2014**, *13*, 897−903.

(6) Dkhissi, Y.; Meyer, S.; Chen, D.; Weerasinghe, H. C.; Spiccia, L.; Cheng, Y. B.; Caruso, R. A. Stability Comparison of Perovskite Solar Cells Based on Zinc Oxide and Titania on Polymer Substrates. *ChemSusChem* **2016**, *9*, 687−695.

(7) Anaraki, E. H.; Kermanpur, A.; Steier, L.; Domanski, K.; Matsui, T.; Tress, W.; Saliba, M.; Abate, A.; Grätzel, M.; Hagfeldt, A.; Correa-Baena, J.-P. Highly Efficient and Stable Planar Perovskite Solar Cells by Solution-Processed Tin Oxide. *Energy Environ. Sci.* **2016**, *9*, 3128−3134.

(8) Wang, Z.; McMeekin, D. P.; Sakai, N.; van Reenen, S.; Wojciechowski, K.; Patel, J. B.; Johnston, M. B.; Snaith, H. J. Efficient and Air-Stable Mixed-Cation Lead Mixed-Halide Perovskite Solar Cells with N-Doped Organic Electron Extraction Layers. *Adv. Mater.* **2017**, *29*, 1604186.

(9) Christians, J. A.; Schulz, P.; Tinkham, J. S.; Schloemer, T. H.; Harvey, S. P.; Tremolet de Villers, B. J.; Berry, A.; Luther, J. J.; Luther, J. M. Tailored Interfaces of Unencapsulated Perovskite Solar Cells for> 1,000 Hour Operational Stability. *Nat. Energy* **2018**, *3*, 68−74.

(10) Ge, C.; Xue, Y. Z. B.; Li, L.; Tang, B.; Hu, H. Recent Progress in 2d/3d Multidimensional Metal Halide Perovskites Solar Cells. *Front. Mater.* **2020**, *7*, 601179.

(11) Al-Ashouri, A.; Magomedov, A.; Roß, M.; Jošt, M.; Talaikis, M.; Chistiakova, G.; Bertram, T.; Márquez, J. A.; Köhnen, E.; Kasparavičius, E.; Levcenco, S.; Gil-Escrig, L.; Hages, C. J.; Schlatmann, R.; Rech, B.; Malinauskas, T.; Unold, T.; Kaufmann, C. A.; Korte, L.; Niaura, G.; Getautis, V.; Albrecht, S. Conformal Monolayer Contacts with Lossless Interfaces for Perovskite Single Junction and Monolithic Tandem Solar Cells. *Energy Environ. Sci.* **2019**, *12*, 3356−3369.

(12) Domanski, K.; Alharbi, E. A.; Hagfeldt, A.; Grätzel, M.; Tress, W. Systematic Investigation of the Impact of Operation Conditions on the Degradation Behaviour of Perovskite Solar Cells. *Nat. Energy* **2018**, *3*, 61−67.

(13) Domanski, K.; Roose, B.; Matsui, T.; Saliba, M.; Turren-Cruz, S.-H.; Correa-Baena, J.-P.; Carmona, C. R.; Richardson, G.; Foster, J. M.; De Angelis, F.; Ball, J. M.; Petrozza, A.; Mine, N.; Nazeeruddin, M. K.; Tress, W.; Grätzel, M.; Steiner, U.; Hagfeldt, A.; Abate, A. Migration of Cations Induces Reversible Performance Losses over Day/Night Cycling in Perovskite Solar Cells. *Energy Environ. Sci.* **2017**, *10*, 604−613.

(14) Ono, L. K.; Qi, Y. Research progress on organic-inorganic halide perovskite materials and solar cells. *J. Phys. D: Appl. Phys.* **2018**, *51*, 093001.

(15) Saliba, M.; Matsui, T.; Seo, J.-Y.; Domanski, K.; Correa-Baena, J.-P.; Nazeeruddin, M. K.; Zakeeruddin, S. M.; Tress, W.; Abate, A.; Hagfeldt, A.; Grätzel, M. Cesium-Containing Triple Cation Perovskite Solar Cells: Improved Stability, Reproducibility and High Efficiency. *Energy Environ. Sci.* **2016**, *9*, 1989−1997.

(16) Hawash, Z.; Ono, L. K.; Qi, Y. Recent Advances in Spiro-Meotad Hole Transport Material and Its Applications in Organic−Inorganic Halide Perovskite Solar Cells. *Adv. Mater. Interfaces* **2018**, *5*, 1700623.

(17) Wang, S.; Sina, M.; Parikh, P.; Uekert, T.; Shahbazian, B.; Devaraj, A.; Meng, Y. S. Role of 4-Tert-Butylpyridine as a Hole Transport Layer Morphological Controller in Perovskite Solar Cells. *Nano Lett.* **2016**, *16*, 5594−5600.

(18) Marongiu, D.; Saba, M.; Quochi, F.; Mura, A.; Bongiovanni, G. The Role of Excitons in 3d and 2d Lead Halide Perovskites. *J. Mater. Chem. C* **2019**, *7*, 12006−12018.

(19) Baranowski, M.; Plochocka, P. Excitons in Metal-Halide Perovskites. *Adv. Energy Mater.* **2020**, *10*, 1903659.

(20) Even, J.; Pedesseau, L.; Katan, C. Analysis of Multivalley and Multibandgap Absorption and Enhancement of Free Carriers Related to Exciton Screening in Hybrid Perovskites. *J. Phys. Chem. C* **2014**, *118*, 11566−11572.

(21) Saba, M.; Cadelano, M.; Marongiu, D.; Chen, F.; Sarritzu, V.; Sestu, N.; Figus, C.; Aresti, M.; Piras, R.; Geddo Lehmann, A. G.; Cannas, C.; Musinu, A.; Quochi, F.; Mura, A.; Bongiovanni, G. Correlated Electron−Hole Plasma in Organometal Perovskites. *Nat. Commun.* **2014**, *5*, 5049.
(22) Yang, Y.; Yan, Y.; Yang, M.; Choi, S.; Zhu, K.; Luther, J. M.; Beard, M. C. Low Surface Recombination Velocity in Solution-Grown Ch3nh3pbbr3 Perovskite Single Crystal. *Nat. Commun.* **2015**, *6*, 7961.
(23) Yang, Y.; Ostrowski, D. P.; France, R. M.; Zhu, K.; van de Lagemaat, J.; Luther, J. M.; Beard, M. C. Observation of a Hot-Phonon Bottleneck in Lead-Iodide Perovskites. *Nat. Photonics* **2016**, *10*, 53−59.
(24) Panzer, F.; Li, C.; Meier, T.; Köhler, A.; Huettner, S. Impact of Structural Dynamics on the Optical Properties of Methylammonium Lead Iodide Perovskites. *Adv. Energy Mater.* **2017**, *7*, 1700286.
(25) Durant, B. K.; Afshari, H.; Singh, S.; Rout, B.; Eperon, G. E.; Sellers, I. R. Tolerance of Perovskite Solar Cells to Targeted Proton Irradiation and Electronic Ionization Induced Healing. *ACS Energy Lett.* **2021**, *6*, 2362−2368.
(26) Lang, F.; Nickel, N. H.; Bundesmann, J.; Seidel, S.; Denker, A.; Albrecht, S.; Brus, V. V.; Rappich, J.; Rech, B.; Landi, G.; Neitzert, H. C. Radiation Hardness and Self-Healing of Perovskite Solar Cells. *Adv. Mater.* **2016**, *28*, 8726−8731.
(27) Brus, V. V.; Lang, F.; Bundesmann, J.; Seidel, S.; Denker, A.; Rech, B.; Landi, G.; Neitzert, H. C.; Rappich, J.; Nickel, N. H. Defect Dynamics in Proton Irradiated Ch3nh3pbi3 Perovskite Solar Cells. *Adv. Electron. Mater.* **2017**, *3*, 1600438.
(28) Kanaya, S.; Kim, G. M.; Ikegami, M.; Miyasaka, T.; Suzuki, K.; Miyazawa, Y.; Toyota, H.; Osonoe, K.; Yamamoto, T.; Hirose, K. Proton Irradiation Tolerance of High-Efficiency Perovskite Absorbers for Space Applications. *J. Phys. Chem. Lett.* **2019**, *10*, 6990−6995.
(29) Moot, T.; Patel, J. B.; McAndrews, G.; Wolf, E. J.; Morales, D.; Gould, I. E.; Rosales, B. A.; Boyd, C. C.; Wheeler, L. M.; Parilla, P. A.; Johnston, S. W.; Schelhas, L. T.; McGehee, M. D.; Luther, J. M. Temperature Coefficients of Perovskite Photovoltaics for Energy Yield Calculations. *ACS Energy Lett.* **2021**, *6*, 2038−2047.
(30) Hoang, M. T.; Yang, Y.; Tuten, B.; Wang, H. Are Metal Halide Perovskite Solar Cells Ready for Space Applications? *J. Phys. Chem. Lett.* **2022**, *13*, 2908−2920.
(31) Brown, C.; Eperon, G.; Whiteside, V.; Sellers, I. Potential of High-Stability Perovskite Solar Cells for Low-Intensity−Low-Temperature (Lilt) Outer Planetary Space Missions. *ACS Appl. Energy Mater.* **2018**, *2*, 814−821.
(32) Hu, S.; Otsuka, K.; Murdey, R.; Nakamura, T.; Truong, M. A.; Yamada, T.; Handa, T.; Matsuda, K.; Nakano, K.; Sato, A. Optimized Carrier Extraction at Interfaces for 23.6% Efficient Tin−Lead Perovskite Solar Cells. *Energy Environ. Sci.* **2022**, *15*, 2096−2107.
(33) Saive, R. S-Shaped Current−Voltage Characteristics in Solar Cells: A Review. *IEEE J. Photovoltaics* **2019**, *9*, 1477−1484.
(34) Roland, P. J.; Bhandari, K. P.; Ellingson, R. J. In Electronic Circuit Model for Evaluating S-Kink Distorted Current-Voltage Curves, *2016 IEEE 43rd Photovoltaic Specialists Conference (PVSC)*, 2016; pp 3091−3094.
(35) Guo, Y.; Yaffe, O.; Hull, T. D.; Owen, J. S.; Reichman, D. R.; Brus, L. E. Dynamic Emission Stokes Shift and Liquid-Like Dielectric Solvation of Band Edge Carriers in Lead-Halide Perovskites. *Nat. Commun.* **2019**, *10*, 1−8.
(36) Lin, L.; Ravindra, N. Temperature Dependence of Cigs and Perovskite Solar Cell Performance: An Overview. *SN Appl. Sci.* **2020**, *2*, 1−12.
(37) Durant, B. K.; Afshari, H.; Sourabh, S.; Yeddu, V.; Bamidele, M. T.; Singh, S.; Rout, B.; Eperon, G. E.; Kim, I. R.; Sellers, I. R. Radiation Stability of Mixed Tin−Lead Halide Perovskites: Implications for Space Applications. *Sol. Energy Mater. Sol. Cells* **2021**, *230*, 111232.
(38) He, J.; Li, T.; Liu, X.; Su, H.; Ku, Z.; Zhong, J.; Huang, F.; Peng, Y.; Cheng, Y.-B. Influence of Phase Transition on Stability of Perovskite Solar Cells under Thermal Cycling Conditions. *Sol. Energy* **2019**, *188*, 312−317.
(39) Parrott, E. S.; Milot, R. L.; Stergiopoulos, T.; Snaith, H. J.; Johnston, M. B.; Herz, L. M. Effect of Structural Phase Transition on Charge-Carrier Lifetimes and Defects in Ch3nh3sni3 Perovskite. *J. Phys. Chem. Lett.* **2016**, *7*, 1321−1326.
(40) Schelhas, L. T.; Christians, J. A.; Berry, J. J.; Toney, M. F.; Tassone, C. J.; Luther, J. M.; Stone, K. H. Monitoring a Silent Phase Transition in Ch3nh3pbi3 Solar Cells Via Operando X-Ray Diffraction. *ACS Energy Lett.* **2016**, *1*, 1007−1012.
(41) Brown, C. R.; Eperon, G. E.; Whiteside, V. R.; Sellers, I. R. Potential of High-Stability Perovskite Solar Cells for Low-Intensity−Low-Temperature (Lilt) Outer Planetary Space Missions. *ACS Appl. Energy Mater.* **2019**, *2*, 814−821.
(42) Sourabh, S.; Whiteside, V.; Sellers, I.; Zhai, Y.; Wang, K.; Beard, M. C.; Yeddu, V.; Bamidele, M.; Kim, D. Hot Carrier Redistribution, Electron-Phonon Interaction, and Their Role in Carrier Relaxation in Thin Film Metal-Halide Perovskites. *Phys. Rev. Mater.* **2021**, *5*, 095402.
(43) Frost, J. M.; Whalley, L. D.; Walsh, A. Slow Cooling of Hot Polarons in Halide Perovskite Solar Cells. *ACS Energy Lett.* **2017**, *2*, 2647−2652.
(44) Ghosh, D.; Welch, E.; Neukirch, A. J.; Zakhidov, A.; Tretiak, S. Polarons in Halide Perovskites: A Perspective. *J. Phys. Chem. Lett.* **2020**, *11*, 3271−3286.
(45) Buizza, L. R.; Herz, L. M. Polarons and Charge Localization in Metal-Halide Semiconductors for Photovoltaic and Light-Emitting Devices. *Adv. Mater.* **2021**, *33*, 2007057.
(46) Schilcher, M. J.; Robinson, P. J.; Abramovitch, D. J.; Tan, L. Z.; Rappe, A. M.; Reichman, D. R.; Egger, D. A. The Significance of Polarons and Dynamic Disorder in Halide Perovskites. *ACS Energy Lett.* **2021**, *6*, 2162−2173.
(47) Wright, A. D.; Verdi, C.; Milot, R. L.; Eperon, G. E.; Pérez-Osorio, M. A.; Snaith, H. J.; Giustino, F.; Johnston, M. B.; Herz, L. M. Electron−Phonon Coupling in Hybrid Lead Halide Perovskites. *Nat. Commun.* **2016**, *7*, 11755.
(48) Lee, J.; Koteles, E. S.; Vassell, M. Luminescence Linewidths of Excitons in Gaas Quantum Wells Below 150 K. *Phys. Rev. B: Condens. Matter Mater. Phys.* **1986**, *33*, 5512.
(49) Veliadis, J. V. D.; Khurgin, J. B.; Ding, Y. J.; Cui, A. G.; Katzer, D. S. Investigation of the Photoluminescence-Linewidth Broadening in Periodic Multiple Narrow Asymmetric Coupled Quantum Wells. *Phys. Rev. B: Condens. Matter Mater. Phys.* **1994**, *50*, 4463−4469.
(50) Chen, X.; Lu, H.; Yang, Y.; Beard, M. C. Excitonic Effects in Methylammonium Lead Halide Perovskites. *J. Phys. Chem. Lett.* **2018**, *9*, 2595−2603.
(51) Miyata, A.; Mitioglu, A.; Plochocka, P.; Portugall, O.; Wang, J. T.-W.; Stranks, S. D.; Snaith, H. J.; Nicholas, R. J. Direct Measurement of the Exciton Binding Energy and Effective Masses for Charge Carriers in Organic−Inorganic Tri-Halide Perovskites. *Nat. Phys.* **2015**, *11*, 582−587.
(52) Ruf, F.; Aygüler, M. F.; Giesbrecht, N.; Rendenbach, B.; Magin, A.; Docampo, P.; Kalt, H.; Hetterich, M. Temperature-Dependent Studies of Exciton Binding Energy and Phase-Transition Suppression in (Cs, Fa, Ma) Pb (I, Br) 3 Perovskites. *APL Mater.* **2019**, *7*, 031113.

https://doi.org/10.1021/acsami.2c11657
ACS Appl. Mater. Interfaces XXXX, XXX, XXX−XXX